

# High-fidelity Multi-view Normal Integration with Scale-encoded Neural Surface Representation

Tongyu Yang<sup>†1</sup> , Heng Guo<sup>†2,4</sup> , Yasuyuki Matsushita<sup>3</sup> , Fumio Okura<sup>3</sup> , Yu Luo<sup>1</sup>, Xin Fan<sup>1</sup> 

<sup>1</sup>Dalian University of Technology, China

<sup>2</sup>Beijing University of Posts and Telecommunications, China

<sup>3</sup>The University of Osaka, Japan

<sup>4</sup>Beijing Key Laboratory of Multimodal Data Intelligent Perception and Governance

---

## Abstract

Previous multi-view normal integration methods typically sample a single ray per pixel, without considering the spatial area covered by each pixel, which varies with camera intrinsics and the camera-to-object distance. Consequently, when the target object is captured at different distances, the normals at corresponding pixels may differ across views. This multi-view surface normal inconsistency results in the blurring of high-frequency details in the reconstructed surface. To address this issue, we propose a scale-encoded neural surface representation that incorporates the pixel coverage area into the neural representation. By associating each 3D point with a spatial scale and calculating its normal from a hybrid grid-based encoding, our method effectively represents multi-scale surface normals captured at varying distances. Furthermore, to enable scale-aware surface reconstruction, we introduce a mesh extraction module that assigns an optimal local scale to each vertex based on the training observations. Experimental results demonstrate that our approach consistently yields high-fidelity surface reconstruction from normals observed at varying distances, outperforming existing multi-view normal integration methods.

---

## 1. Introduction

Detailed 3D surface reconstruction is essential for a wide range of applications, including 3D printing, virtual reality, and cultural heritage preservation [KPL25, LBTZ24]. Multi-view normal integration is a fundamental method for 3D reconstruction, enabling detailed surface geometry recovery given multi-view normal maps and camera poses, typically as a subsequent step to photometric stereo (PS) [LZW\*20, WRG\*23].

Existing multi-view normal integration methods [XT24, BBQ\*24] demonstrate a strong ability to represent high-frequency signals. They adopt a point-sampling strategy [MESK22, WHH\*23], where each pixel is treated as a single point without accounting for the actual area it covers (which is determined by camera intrinsics and the camera-to-object distance). Consequently, they generally assume that the images are captured under the same camera-to-object distance with consistent intrinsics, so that the spatial resolution (i.e., the area size corresponding to each pixel) of surface normals across different views is roughly comparable. However, when the camera distances vary across views, the same region may correspond to different 2D normal distributions, leading to scale-induced inconsistencies among multi-view observations.

This motivates the need to explicitly incorporate scale information in the shape representation for high-fidelity 3D reconstruction.

In real-world image acquisition, high-frequency details are often concentrated in local regions. To capture them effectively, close-up shots are employed for detail-rich areas, while long shots are used to record the global geometry. Figure 1 (a) provides such an example: long shots capture the overall contour of the object as regular views, whereas close-up views reveal the fine structures of the microphone head. When zooming in on the normals of the same surface region across different views, noticeable inconsistencies emerge, as the recorded pixel normals correspond to different spatial resolutions of the same underlying surface area.

Existing multi-scale representation-based novel view synthesis (NVS) methods [BMT\*21, HWM\*23] that take RGB images as input have successfully alleviated the multi-view inconsistencies caused by scale variations. For example, the integrated positional encoding (IPE) encoding in Mip-NeRF [BMT\*21] approximates frustums with Gaussian distributions. However, these methods [BMV\*23, LHY\*24] are primarily designed to improve 2D NVS quality at arbitrary scales, rather than to ensure the geometric accuracy of 3D reconstruction, which involves a neural surface-constrained representation followed by mesh extraction. In particular, they fail to achieve a scale-aware mesh from a surface-constrained representation, since the scale of each spatial point is no longer determined from 2D observations. Adopting a single

---

<sup>†</sup> These authors contributed equally.

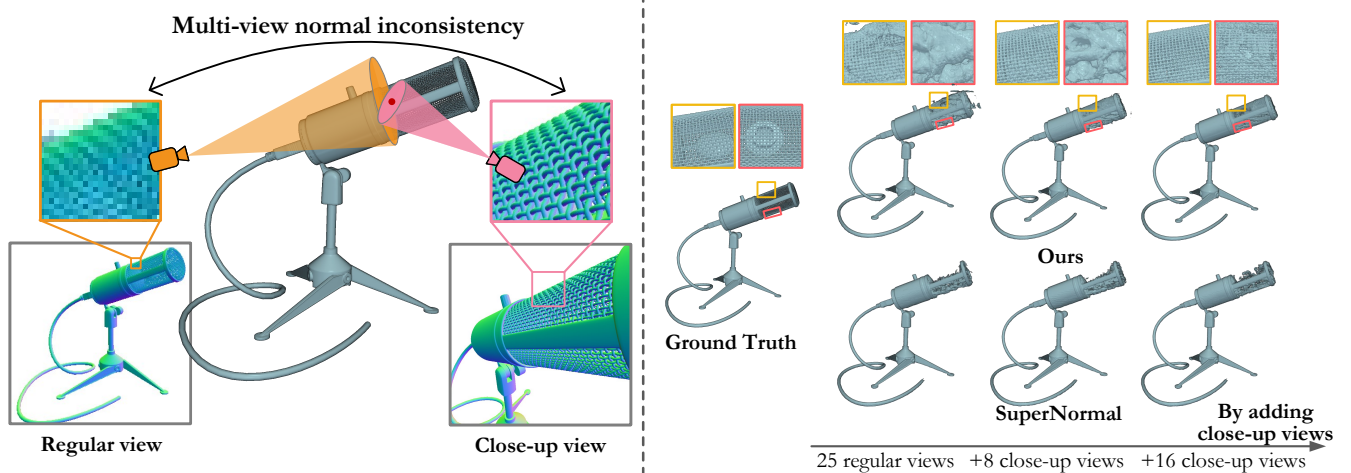


**Figure 1:** (a) Problem setup: Given surface normals captured at varying scales, the goal is to recover detailed 3D surfaces while addressing multi-view inconsistencies caused by scale variations. (b) Comparison with Existing Method [XT24]: Our approach can handle surface normal inputs at multiple scales (close-up and regular), enabling the recovery of fine surface details, particularly in high-frequency regions.

global scale for mesh extraction can lead to suboptimal outcomes: using a large scale tends to over-smooth fine local details captured by multi-scale observations, whereas using a small scale often produces unreliable meshes due to insufficient observation in most regions. This problem becomes particularly pronounced when the training dataset contains images captured from varying distances. To achieve high-quality geometric reconstruction, it is crucial to assign to each spatial location the most reliable local scale during mesh extraction so that fine details revealed by close-up views can be preserved.

Motivated by the need for scale-aware reconstruction, we introduce a scale-encoded neural surface representation (SNSR) that addresses multi-view normal inconsistency caused by scale variations in the normal maps, enabling scale handling in both multi-view normal integration optimization and mesh extraction. It allows for high-fidelity multi-view normal integration across both close-up and global-shot surface normals. Figure 1 (b) illustrates the overall geometry of the microphone can be reconstructed with only regular views, but fine details are missing. As close-up views are gradually added, more detailed structures of the microphone emerge. In contrast, since the details among normals at different scales are blurred by point-based methods such as SuperNormal [XT24], they fail to effectively capture these fine-grained local structures.

Specifically, to handle multiscale surface normal input, SNSR encodes scale associated with each position into features. This approach models the surface normal as a function of scale, allowing each position to extract features at various scales. To achieve this, we sample spheres instead of points and incorporate each sphere’s scale along the ray as an additional input. Furthermore, since incorporating scale results in a sparser representation, we introduce a cross-scale regularization (CSR) loss to regularize signed distance function (SDF) values across scales. Finally, to determine the scale of each point during surface extraction, we introduce an SNSR-based mesh extraction module (SMEM), which leverages

the learned SNSR feature map to infer the well-trained scale corresponding to each position, enabling scale-aware mesh reconstruction. Our contributions are summarized as follows:

- We propose a scale-encoded neural surface representation (SNSR) to resolve surface normal inconsistencies under large variations in spatial resolution;
- We present an SNSR-based mesh extraction module (SMEM) that enables scale-aware mesh extraction while preserving fine-grained geometric details;
- Experiments show that our method effectively handles multi-scale surface normals, enabling detailed reconstruction.

## 2. Related Works

This work focuses on multi-scale representation-based normal integration from multi-view normal maps. In the following, Sec. 2.1 reviews related works on single-view and multi-view normal integration methods. Section 2.2 surveys multi-scale representation methods for arbitrary-resolution rendering based on different underlying forms.

### 2.1. Surface normal integration

Normal integration refers to reconstructing a surface from a given normal field by solving for a scalar function whose gradient is consistent with the observed normals [HZ24, QDA18].

In the single-view setting, the task reduces to integrating a single normal map. Classical approaches either formulate the problem as solving a Poisson equation [HB86] or directly discretize the energy functional [DC07]. Both cases lead to a linear system of equations. To tackle blurred depth discontinuities in normal integration, Cao *et al.* [CSS\*22] assume the surface is one-sided differentiable everywhere in the horizontal and vertical directions, and

propose a bilaterally weighted normal integration functional to preserve discontinuities. More recent works focus on improving efficiency by moving beyond regular pixel grids, for instance, through adaptive meshing [HZ24] or mesh decimation strategies [HBZ25], while also preserving fine geometric details.

To extend normal integration to multiple views, recent approaches adopt implicit neural representations and differentiable rendering. SuperNormal [XT24] employs directional finite differences and patch-based ray marching to approximate signed distance function (SDF) gradients, aiming for fine-grained surface details and efficiency. RNb-NeuS [BBQ\*24] reparameterizes reflectance and normals as radiance vectors under varying illumination, targeting improved multi-view reconstruction. PMNI [PCW\*25] utilizes multi-view surface normals as geometric cues, jointly estimating camera poses and surface geometry. It improves reconstruction quality on reflective and textureless surfaces without requiring reliable initial poses.

However, these multi-view normal integration methods typically assume that normal maps are captured from roughly a constant distance from the object. When images are captured from varying distances, these methods treat each pixel as a single point instead of an area, which leads to ambiguity when different spatial resolutions are present at the same position, significantly limiting their performance.

## 2.2. Multiscale 3D neural representation

Multiscale representation enables models to render high-quality images at arbitrary scales. Achieving this requires explicitly accounting for the spatial resolution of pixels during rendering to ensure geometric and appearance consistency across different scales. Early point-sampled models (*e.g.*, NeRF [MST\*20]) do not explicitly model spatial resolution, which makes them prone to performance degradation when there is a mismatch between training and testing resolutions, thus limiting their ability to support stable cross-scale rendering. To address this issue, a variety of multiscale representation approaches have been proposed, which can be broadly categorized into three types: NeRF-based representations, SDF-based representations, and 3DGS-based representations.

**NeRF-based representation.** Mip-NeRF [BMT\*21] extends NeRF [MST\*20] by casting cones instead of rays, and uses 3D Gaussians to approximate the conical frustums of each pixel as the integrated positional encoding (IPE). To prevent aliasing in hybrid representation models [MESK22], Zip-NeRF [BMV\*23] adopts a multi-sampling-based strategy to approximate the average NGP [MESK22] feature over a conical frustum. By comparison, Tri-MipRF [HWM\*23] adopts a pre-filtering approach by emitting cones from the camera to the image plane, sampling spheres within each cone, and using TriMip encoding to represent each sphere. Rip-NeRF [LHY\*24] further improves Tri-MipRF [HWM\*23] with isotropic area sampling.

**SDF-based representation.** Despite providing implicit neural representations for NVS, NeRF-based methods struggle to extract high-quality surfaces due to soft density. NeuS [WLL\*21] and its variants [WSW23, WSW22] introduce neural SDFs for smoother and more detailed reconstructions, yet ray sampling still

limits adaptive capture of varying detail across regions. To enable anti-aliased rendering and recover delicate geometric features, LoD-NeuS [ZZF\*23] aggregates spatial features via multi-convolved featurization within a conical frustum along a ray. RING-NeRF [PBP\*24] introduces two key inductive biases: a continuous multi-scale representation and a decoder latent space invariant to both spatial location and scale, addressing NeRF’s common challenges such as robustness, handling unbounded scenes, and adaptive NVS.

**3DGS-based representation.** Currently, 3D Gaussian Splatting (3DGS) [KKLD23, LWZ\*24] is notable for its real-time rendering. However, a strong artifact is observed when changing the sampling rate. Analytic-Splatting [LZH\*24] addresses aliasing by expanding each pixel integration area, enhancing sensitivity to spatial resolution variations of pixels across resolutions in 3DGS [KKLD23]. Mip-Splatting [YCH\*24] uses a 3D smoothing filter combined with a 2D Mip filter to reduce high-frequency artifacts. Due to the discrete nature and the multi-view inconsistent behavior of 3D Gaussians, 3DGS [KKLD23] is difficult to directly apply for surface reconstruction. Some works [ZYW25, HYC\*24] have explored surface reconstruction based on 3DGS representation, but they do not leverage a multi-scale representation.

The above-mentioned methods primarily focus on NVS, where the scale can be directly inferred from 2D observations. However, they do not consider scale during mesh extraction, where the optimal local scale cannot be directly determined. In contrast, aiming at high-quality 3D reconstruction, we propose a multi-scale representation and extend it with SMEM, enabling scale-aware mesh extraction and the recovery of high-fidelity geometric details.

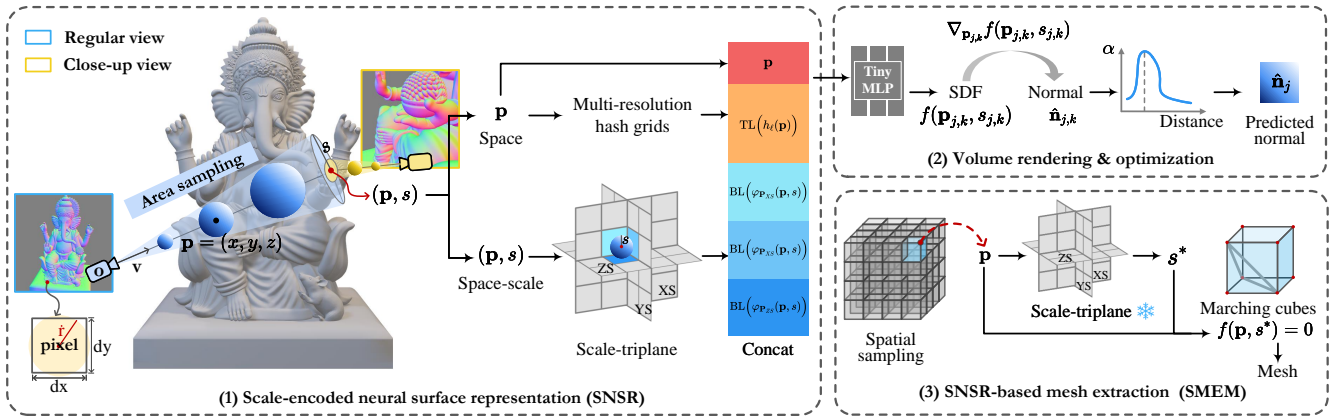
## 3. Proposed Method

Figure 2 shows an overview of our method. For multi-view normal maps captured at varying distances, we first adopt a sphere-based area sampling strategy, representing each sampled region by its center position and radius. These position and scale parameters are then fed into hash grids and the scale-triplane module to obtain multi-scale feature representations. Next, surface normals along each ray are computed via volume rendering. The representation is optimized by a composite loss, including our proposed  $\mathcal{L}_{CSR}$ . During mesh extraction, we further introduce SMEM, an adaptive scale selection strategy to determine the optimal training-time scale for each vertex, enabling high-fidelity mesh reconstruction.

### 3.1. Scale-encoded neural surface representation

Given two types of normal maps captured at different distances, as shown in Fig. 2: regular view captures the overall shape of the object, and close-up view focuses on high-frequency details. The observation scales associated with these two views differ significantly, and neglecting this difference can lead to multi-view normal inconsistencies during optimization.

To represent positions  $\mathbf{p} = (x, y, z) \in \mathbb{R}^3$  as areas rather than individual points, we follow Tri-MipRF [HWM\*23], casting a cone from the camera center  $\mathbf{o}$  along the direction  $\mathbf{v}$  and sampling inscribed spheres within the cone. The center position of each sam-



**Figure 2: Method overview.** (1) We sample inscribed spheres within the cone, each with position  $\mathbf{p}$  and scale  $s$ , which are jointly encoded via hash grids and a scale-triplane. Interpolated features are concatenated and fed into a tiny MLP to output SDF and surface normal. (2) Pixel normals are computed via volume rendering. (3) SMEM enables mesh extraction at the optimal scale.

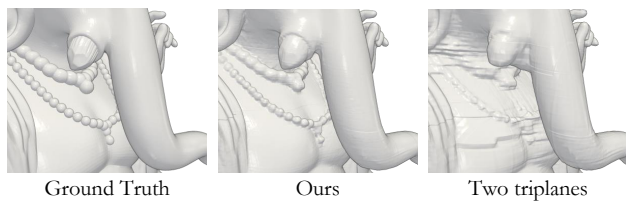


**Figure 3: Comparison between our hybrid representation and two triplanes.** Both methods use multi-resolution grids with the same finest spatial resolution.

pled sphere is given by:

$$\mathbf{p} = \mathbf{o} + t\mathbf{v}, \tag{1}$$

where  $t$  denotes the sampling distance along the ray. The radius  $s$  of each sphere encodes the scale of the corresponding point, which can be calculated as [HWM\*23]:

$$s = \frac{\|\mathbf{p} - \mathbf{o}\|_2 \cdot F \cdot \dot{r}}{\|\mathbf{v}\|_2 \cdot \sqrt{(\sqrt{\|\mathbf{v}\|_2^2 - F^2} - \dot{r})^2 + F^2}}, \tag{2}$$

where  $F$  denotes the focal length, and  $\dot{r}$  is the scale of the disc on the image plane, computed as

$$\dot{r} = \sqrt{\frac{dy \cdot dx}{\pi}}, \tag{3}$$

where  $dx$  and  $dy$  are the width and height of the pixel in world coordinates that can be calculated from the camera intrinsics.

After obtaining the scale, each point can be represented as a 4D coordinate  $(\mathbf{p}, s)$ . Two straightforward approaches are possible to encode this coordinate: a full 4D hash grid which replicates a 3D hash grid at each scale, or a decomposition into two triplanes—three planes  $\mathbf{P}_{XY}, \mathbf{P}_{XZ}, \mathbf{P}_{YZ}$  for spatial dimensions and three planes  $\mathbf{P}_{XS}, \mathbf{P}_{YS}, \mathbf{P}_{ZS}$  for scale. However, the former leads to

an excessively large model when scales vary [FKMW\*23], while the latter struggles to capture high-frequency spatial details (Fig. 3).

To leverage the strengths of both representations, we adopt a hybrid multi-scale neural representation: a multi-resolution hash grid encodes spatial positions, while a scale-triplane  $\mathbf{P}_{XS}, \mathbf{P}_{YS}, \mathbf{P}_{ZS}$  encodes the joint position–scale space. This design provides continuous representation across arbitrary scales, explicitly links scale to surface normals, and reduces memory or improves detail representation compared to a full 4D grid or dual-triplane approach. Figure 3 illustrates that our method recovers finer details and requires less time (40 minutes) for the same number of iterations, compared to 120 minutes for the two triplanes representation.

In particular, Fig. 2 illustrates that we input  $\mathbf{p}$  into a multi-resolution hash encoding to obtain spatial features, while  $(\mathbf{p}, s)$  are fed into a single-resolution scale-triplane to capture scale-dependent features. Feature vectors are obtained by linearly interpolating according to the position and scale from the hash encoding and triplane, respectively. Then, we concatenate these features as the input to a tiny MLP, which decodes them into SDF values  $f$ :

$$f(\mathbf{p}, s) = \text{MLP} \left\{ \begin{array}{l} \mathbf{p}, \\ \text{TL}(h_\ell(\mathbf{p})), \ell = \{1 \dots L\}, \\ \text{BL}(\varphi_c(\mathbf{p}, s)), c = \{\mathbf{P}_{XS}, \mathbf{P}_{YS}, \mathbf{P}_{ZS}\} \end{array} \right\}_{\text{concat}}, \tag{4}$$

where TL and BL denote the trilinear and bilinear interpolation operations, respectively,  $h_\ell$  is the  $\ell$ -th level of hash grids, and  $\varphi_c$  projects  $(\mathbf{p}, s)$  onto the  $c$ -th plane.

### 3.2. Volume rendering of surface normal

After obtaining SDF values at sampled points, we compute surface normals along each ray using volume rendering, which allows supervision from the ground-truth normal maps to optimize our multi-scale representation. We adopt PyTorch’s automatic differentiation

approach. For the  $k$ -th sample point along the  $j$ -th ray  $\mathbf{p}_{j,k}$ , its predicted normal  $\hat{\mathbf{n}}_k$  is given by:

$$\hat{\mathbf{n}}_{j,k} = \nabla_{\mathbf{p}_{j,k}} f(\mathbf{p}_{j,k}, s_{j,k}). \quad (5)$$

Then, following NeuS [WLL\*21], we adopt an unbiased and occlusion-aware method to convert SDF samples into volume rendering opacities, allowing us to transform the signed distance values into densities:

$$\alpha_{j,k} = \max \left( \frac{\Phi_a(f(\mathbf{p}_{j,k}, s_{j,k}) - \Phi_a(f(\mathbf{p}_{j,k+1}, s_{j,k+1})), 0)}{\Phi_a(f(\mathbf{p}_{j,k}, s_{j,k}))}, 0 \right), \quad (6)$$

where  $\alpha_{j,k}$  is discrete opacity values, and  $\Phi_a(\cdot) = (1 + e^{-a(\cdot)})^{-1}$  is the sigmoid function with a trainable sharpness parameter  $a$ .

Finally, the normal along the  $j$ -th ray  $\hat{\mathbf{n}}_j$  is computed via volume rendering:

$$\hat{\mathbf{n}}_j = \sum_{k=1}^M T_{j,k} \alpha_{j,k} \hat{\mathbf{n}}_{j,k}, \quad \text{with} \quad T_{j,k} = \prod_{l=1}^{k-1} (1 - \alpha_{j,l}), \quad (7)$$

where  $M$  is the number of the sampled points of each ray.

### 3.3. Loss functions

To optimize our multi-scale representation, we employ the following loss functions.

**Normal loss.** The normal loss encourages the estimated normals  $\hat{\mathbf{n}}$  to align with the input normal vectors  $\mathbf{n}$ , thereby facilitating the recovery of accurate geometric details:

$$\mathcal{L}_{\text{normal}} = \frac{1}{N} \sum_{j=1}^N \|\hat{\mathbf{n}}_j - \mathbf{n}_j\|_1, \quad (8)$$

where  $N$  is the number of rays.

**Mask loss.** The mask term aligns the shape's silhouette with the input masks, serving as a boundary condition.

$$\mathcal{L}_{\text{mask}} = -\frac{1}{N} \sum_{j=1}^N \left[ m_j \log(\hat{m}_j) + (1 - m_j) \log(1 - \hat{m}_j) \right], \quad (9)$$

where  $\hat{m}_j = \sum_{k=1}^M T_{j,k} \alpha_{j,k}$  denotes the accumulated opacity along the  $j$ -th ray, and  $m_j \in \{0, 1\}$  denotes the ground-truth binary mask value at the  $j$ -th pixel.

**Eikonal loss.** Eikonal loss [OFP04] constrains the gradient norm of the SDF to be close to 1 throughout the space, ensuring that the neural SDF remains a valid representation of the surface geometry.

$$\mathcal{L}_{\text{eikonal}} = \frac{1}{NM} \sum_{j,k} (\|\nabla_{\mathbf{p}_{j,k}} f(\mathbf{p}_{j,k}, s_{j,k})\|_2 - 1)^2. \quad (10)$$

**Cross-Scale regularization loss.** The additional scale input makes our method more prone to overfitting the normal maps, resulting in high-quality normal maps but inaccurate depth estimations (as shown in Fig. 10, row 1, column 2 and 3). This, in turn, negatively impacts mesh generation. The issue arises because not all regions appear in close-up views, *i.e.*, not all points have been observed at smaller scales. For these unobserved scales, there is

no corresponding supervision for optimization. Therefore, we introduce an unsupervised Cross-Scale regularization term  $\mathcal{L}_{\text{CSR}}$  to associate the SDF values at these scales with the reliably trained SDF, and prevent the model from over-fitting. Specifically, in each iteration, we randomly select  $K$  sampled points and uniformly sample  $S$  scales within the range between the minimum and maximum radius. It is worth noting that only a small number of points and scales are required to perform this regularization effectively.

$$\mathcal{L}_{\text{CSR}} = \frac{1}{KS} \sum_{k=1}^K \sum_{i=1}^S \|f(\mathbf{p}_k, s_{k,i}) - \mu_k\|_2^2, \quad (11)$$

$$\text{with} \quad \mu_k = \frac{1}{S} \sum_{i=1}^S f(\mathbf{p}_k, s_{k,i}).$$

**Overall loss.** The overall loss function is given by:

$$\mathcal{L} = \mathcal{L}_{\text{normal}} + \mathcal{L}_{\text{mask}} + \mathcal{L}_{\text{eikonal}} + \lambda \mathcal{L}_{\text{CSR}}, \quad (12)$$

where  $\lambda$  denotes the weight of  $\mathcal{L}_{\text{CSR}}$ .

### 3.4. SNSR-based mesh extraction

To extract mesh from the SDF, we define the surface  $\mathcal{S}$  as the zero-level set of the SDF  $f$ :

$$\mathcal{S} = \left\{ (\mathbf{p}, s) \in \mathbb{R}^4 \mid f(\mathbf{p}, s) = 0 \right\}. \quad (13)$$

During training, each point is assigned an optimal scale based on its view, allowing the model to learn with the most suitable scale for each position. Ideally, these learned scales could guide mesh extraction to recover the most detailed geometry. However, since mesh extraction is independent of the observed images, the scale corresponding to the finest SDF at each spatial location cannot be directly determined, making it challenging to reconstruct a high-fidelity 3D mesh. To address this, we design an SNSR-based mesh extraction module (SMEM) to adaptively find the optimal scale for each vertex with the marching cubes algorithm [LC98].

Since the optimal scale used for mesh extraction is derived from the training observations, we can naturally obtain the scale of each vertex from the trained scale-triplane feature map. We visualize this feature map in Fig. 4 and observe that the maximum value on the triplane aligns with the well-trained scale. This phenomenon can be explained by the initialization of the triplane features with zeros: scales that are rarely observed tend to remain close to zero, whereas positions that are sufficiently constrained by multi-view observations accumulate stronger activations during training, resulting in higher feature values. Consequently, the maximum response over scales at a given position naturally indicates the scale at which the representation has been most effectively learned.

Figure 4 depicts the flowchart of our SMEM. Based on this observation, we first query each vertex on the three planes  $\mathbf{P}_{XS}, \mathbf{P}_{YS}, \mathbf{P}_{ZS}$  to obtain three sets of feature values corresponding to the  $X, Y,$  and  $Z$  coordinates, covering all the scales involved in training for that vertex. Since the maximum feature responses along the three axes do not necessarily correspond to the same scale, while the training process consistently optimizes all three axes at a shared scale, we sum the three feature values to identify the scale

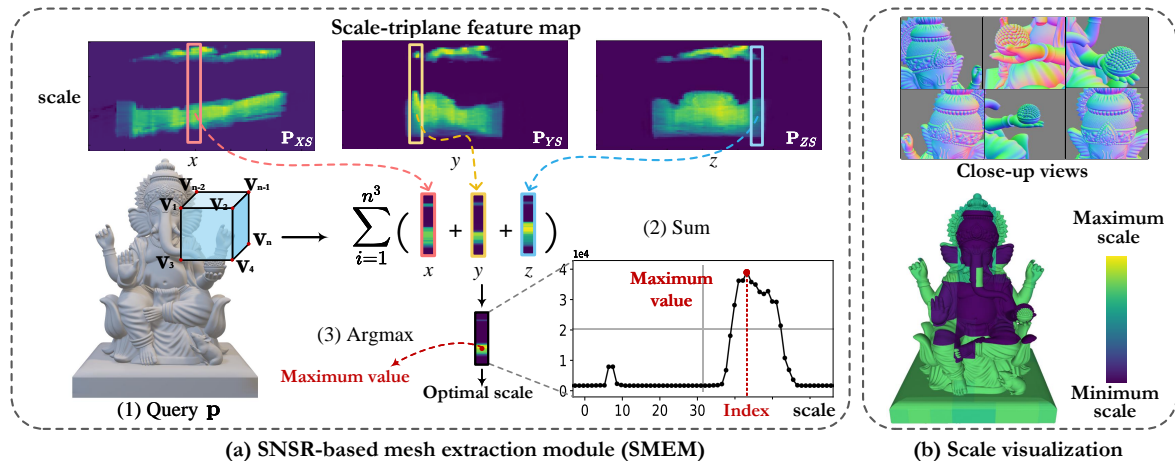


**Figure 4:** The flowchart of SMEM. (a) For each vertex within a cell, we query the scale-triplane feature map at its position  $\mathbf{p}$ , sum the features of  $x$ ,  $y$ , and  $z$  axes for all vertices within the cell, and select the scale with the maximum aggregated response as the cell’s final scale. (b) We visualize the scales on the extracted mesh, where the purple areas correspond to smaller scales, which is consistent with the observations from the close-up views.

that jointly maximizes their responses, which is then selected as the final scale.

Using this insight, we first query each vertex on the feature map to obtain three sets of values, each corresponding to  $x$ ,  $y$ , and  $z$  coordinates, respectively. Since each  $(x, y, z)$  position corresponds to the same scale, we sum  $xs$ ,  $ys$ , and  $zs$  to yield one column of scales per vertex, from which we determine a single optimal scale. The final optimal scale for each vertex is selected by summing these columns and choosing the scale associated with the maximum value from the feature map. We visualize each vertex’s scale on the mesh, as shown in Fig. 4 (b). Purple sections represent regions where a smaller scale is used for mesh extraction, corresponding to close-up view coverage, while other regions apply the scale associated with regular views.

Directly selecting the scale corresponding to the maximum feature value for each vertex may lead to surface discontinuities, as SDF vary significantly across different scales. To mitigate this issue, we partition the entire volume into units  $n \times n \times n$  (with  $n = 64$ ), and assign a consistent scale to all vertices within each unit. The final scale  $s^*$  for each unit volume is calculated by:

$$s^* = \operatorname{argmax}_s \sum_{i=1}^{n^3} \sum_c \operatorname{BL}(\phi_c(\mathbf{p})), c = \{\mathbf{P}_{xS}, \mathbf{P}_{yS}, \mathbf{P}_{zS}\}. \quad (14)$$

**Implementation details.** The input 3D coordinate  $\mathbf{p}$  and scale  $s$  are transformed through our scale-triplane encoding and hash encoding [MESK22] into a 55-dimensional feature vector (3 dimensions from position  $\mathbf{p}$ , 28 dimensions from multi-resolution hash grids, and 24 dimensions from Scale-triplane). The hyperparameter setting of hash grids is the same as SuperNormal [XT24]. Subsequently, a tiny multi-layer perceptron (MLP) with 64 units is used to decode the features, with ReLU activation applied to the single hidden layer. Additionally, the resolution of each plane in the triplane representation is  $128 \times 32$ , where 128 and 32 correspond to

the resolution of the 3D coordinate  $\mathbf{p}$  and scale  $s$ , respectively. We randomly sample 4096 rays per batch, and the total number of iterations is 70,000. We use the Adam optimizer with an initial learning rate  $5 \times 10^{-3}$ . For each iteration, we use 128 rays with 4096 sampled points, and for  $\mathcal{L}_{\text{CSR}}$ , we randomly select 4096 points from it, uniformly sample 128 scales, and set  $\lambda = 4$

## 4. Experiments

In this section, we present a comparison between our method and existing normal integration approaches, and conduct an ablation study to demonstrate the effectiveness of our approach.

### 4.1. Experimental settings

**Datasets.** To compare our method with existing multi-view normal integration approaches, we render synthetic datasets at a resolution of  $800 \times 800$ , containing four high-frequency objects selected from NeRF [MST\*20] and Sketchfab [D.]. For data generation, *Setting I* consists of about 32 normal maps rendered in Blender from a constant distance. *Setting II* augments *Setting I* with an additional with 8 to 16 close-up views that capture fine details which are challenging to observe in regular views. Figure 5 illustrates the camera pose distributions used for normal rendering and examples of regular and close-up views for each object. *Setting I* highlights the benefit of close-up views, while *Setting II* introduces larger multi-view normal inconsistencies. We also render RGB for training rgb-based methods.

For the real-world dataset, since ground-truth normal maps are unavailable, we follow the existing multi-view normal integration approach [XT24], which applies SDM-UniPS [Ike23] to estimate per-view surface normals from images captured under multiple illumination conditions. To this end, we capture images using the

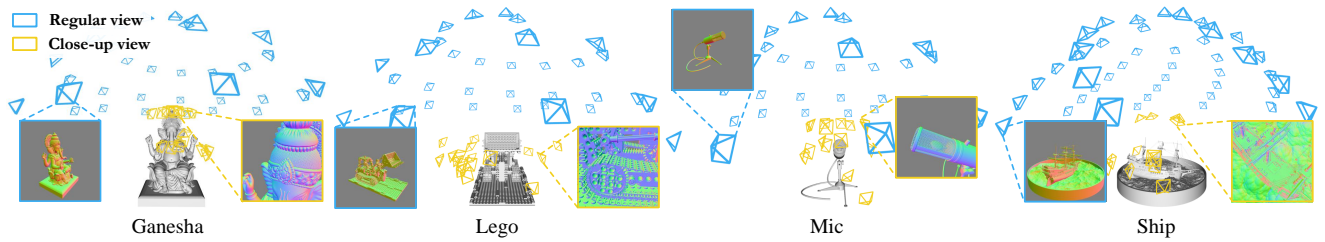


**Figure 5:** Setup of synthetic data generation. Blue and yellow camera poses denote the regular and close-up views, respectively. We provide example views for each object.

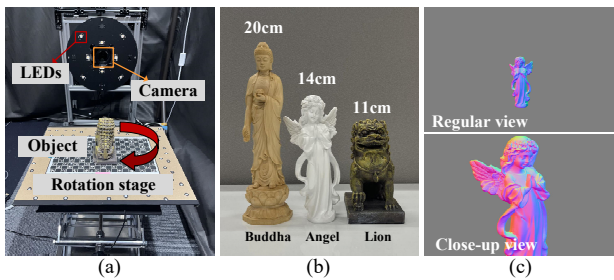


**Figure 6:** Setup of our real-world experiment. (a) The target object is placed on a checkerboard and imaged on a rotation stage under 12 lighting conditions. (b) The objects range in height from 11 cm to 20 cm. (c) Normal maps estimated from SDM-UniPS [Ike23].

setup illustrated in Fig. 6 (a). We select three objects with complex geometric shapes (Fig. 6 (b)), each imaged from 26 view-points (24 regular views and 2 close-up views) under 12 lighting conditions. Images are acquired using a Canon EOS RP at a resolution of  $3360 \times 2240$ . Camera parameters are calibrated with Metashape [Agi24], foreground masks are generated with SAM [KMR\*23].

**Baselines.** Based on high-fidelity 3D reconstruction task, we compare our method with the following categories: (1) *Multi-view normal integration:* SuperNormal [XT24] and RNb-NeuS [BBQ\*24] are state-of-the-art (SOTA) approaches that take the same inputs and produce the same outputs as our method. (2) *Detailed surface reconstruction:* PET-NeuS [WSW23] effectively captures high-frequency details from multi-view RGB images. For a fair comparison, we use both normal maps and RGB images for the training stage. (3) *Multi-scale representation:* Since the code for existing multi-scale representation-based 3D reconstruction methods [ZZF\*23, PBP\*24] is not publicly available, we choose Tri-MipRF [HWM\*23] which is designed for NVS and does not produce normal outputs. Hence, we train it using only RGB images.

**Evaluation metrics.** We use Mean Angular Error (MAE) and L2 Chamfer Distance (CD) [mm] [KKO\*22, KPZK17] to evaluate the accuracy of novel-view normal maps and 3D mesh, respectively.

## 4.2. Comparison on synthetic data

Table 1 shows MAE on six regular views and three close-up views, together with the CD for each object. Visualization results of *Ganesha* and *Lego* are shown in Fig. 7. Comparing the results of setting I and setting II, we observe that incorporating close-up views significantly improves the accuracy of 3D reconstruction, demonstrating the importance of such views for achieving high-quality geometry. However, introducing close-up views also increases scale variations among images and amplifies the influence of multi-view normal inconsistency. Our method explicitly accounts for the spatial coverage of each sampled point and takes the scale as one of the network inputs, leading to a multi-scale representation. This representation better preserves geometric details and mitigates multi-view normal inconsistency, producing renderings that are more consistent with ground truth. Consequently, our approach outperforms all baselines in both MAE and CD metrics.

In contrast, RNb-NeuS [BBQ\*24] exhibits limited capability in capturing fine details, resulting in over-smoothed surfaces. Both SuperNormal [XT24] and PET-NeuS [WSW23] adopt grid-based representations, which improve the modeling of high-frequency signals. However, their lack of multi-scale design makes them susceptible to noise in regions with large scale variations. Tri-MipRF [HWM\*23] projects the sampling scale onto multiple levels to estimate density. Although this constitutes a multi-scale representation, mesh extraction in Tri-MipRF [HWM\*23] suffers from two limitations. First, it can only extract meshes at a single scale, for which we use the finest level from the training stage. This is because Tri-MipRF [HWM\*23] lacks a mechanism to adaptively select the optimal scale for each spatial point, unlike our method which performs scale-adaptive mesh extraction. Second, Tri-MipRF [HWM\*23] represents the scene using a density field, a soft representation that is inherently prone to noise.

For running time, we train each method on a single RTX A6000, with the training time displayed in the last column of Table 1. PET-NeuS [WSW23] takes the longest time due to its self-attention feature extractor, while ours runs slightly slower than SuperNormal [XT24] and Tri-MipRF [HWM\*23] because of additional scale encoding, yet achieves superior geometric accuracy.

## 4.3. Comparison on real-world data

For real-world experiments, we exclude RNb-NeuS [BBQ\*24], as it produces over-smoothed results on synthetic data and requires

**Table 1:** Quantitative evaluation on synthetic data. Red and orange cells indicate *the best* and *the second best* results, respectively. Results are measured in terms of MAE and CD.

Method	Mean Angular Error ↓ (novel views)				L2 Chamfer Distance ↓				Runtime ↓
	Ganesha	Lego	Mic	Ship	Ganesha	Lego	Mic	Ship	
<b>Setting I, only regular views:</b>									
SuperNormal [XT24]	7.5770	16.815	13.551	7.103	0.2577	0.3476	0.1899	0.1516	14 mins
RNb-NeuS [BBQ*24]	7.5810	17.061	14.655	7.648	0.1809	0.5677	0.6132	0.2563	11 hrs
PET-NeuS [WSW23]	6.7042	13.549	18.818	7.149	0.1837	0.2028	0.5415	0.1634	26 hrs
Tri-MipRF [HWM*23]	-	-	-	-	0.5111	0.7477	0.4906	0.6730	13 mins
Ours	4.1205	11.1419	8.5297	4.7417	0.0617	0.1474	0.0812	0.0704	34 mins
<b>Setting II, regular + close-up views:</b>									
SuperNormal [XT24]	6.7823	12.263	12.403	6.664	0.1606	0.1768	0.1601	0.1405	14 mins
RNb-NeuS [BBQ*24]	6.7518	18.47	14.679	7.956	0.1474	0.3504	0.8635	0.3273	11 hrs
PET-NeuS [WSW23]	6.0367	11.7567	14.778	6.871	0.177	0.1477	0.3927	0.1437	26 hrs
Tri-MipRF [HWM*23]	-	-	-	-	0.5608	0.6576	0.7784	0.6947	13 mins
Ours	3.7028	8.8386	7.7164	4.5801	0.0483	0.1131	0.0809	0.0684	34 mins

**Table 2:** Ablation study on SNSR and  $\mathcal{L}_{CSR}$  on synthetic data. **Bold text** indicates the best result.

	Setting I		Setting II	
	MAE ↓	CD ↓	MAE ↓	CD ↓
w/o SNSR	4.622	0.1119	5.342	0.097
w/o $\mathcal{L}_{CSR}$	4.455	0.0687	4.443	0.068
Ours	<b>4.121</b>	<b>0.0617</b>	<b>3.703</b>	<b>0.048</b>

albedo inputs, which are difficult to obtain in real-world scenarios. As shown in Fig. 8, our method reconstructs finer geometric details by effectively utilizing close-up views. By comparison, the meshes produced by other methods tend to degrade when close-up views are included. For instance, SuperNormal [XT24] exhibits lower accuracy on *Angel*, whereas PET-NeuS [WSW23] shows degraded performance on *Lion*. This degradation occurs because point-sampling-based methods exhibit increased multi-view normal inconsistency when close-up views are added. The noise of Tri-MipRF [HWM\*23] is exacerbated on the real-world dataset.

#### 4.4. Ablation study

Table 2, Fig. 9 and Fig. 10, demonstrate the effectiveness of both SNSR and  $\mathcal{L}_{CSR}$ . For SNSR, the improvement is more pronounced in Setting II (regular + close-up views). This is because Setting II involves various scales, and the presence of more scales tends to increase multi-view normal inconsistencies. In contrast, in Setting I (only regular views), since the distance between the camera and the object remains constant, the sampling points share relatively uniform scales. As a result, although the effect is less noticeable, the performance still improves. The role of  $\mathcal{L}_{CSR}$  is to enforce smoother meshes extracted from SNSR. Figure 9 shows that without  $\mathcal{L}_{CSR}$ , the reconstructed meshes exhibit local non-smoothness.

Additionally, Fig. 10 shows that the introduction of  $\mathcal{L}_{CSR}$  helps prevent the model from overfitting.

Table 3 and Fig. 11 illustrate the effectiveness of our proposed SMEM, which requires no additional computation. A straightforward alternative is to search for a globally consistent scale across all vertices over iterations, but this is highly time-consuming. For comparison, we manually set a suitable minimum and maximum scale, uniformly sampled 10 scales within this range, and selected the best-performing mesh for evaluation. As evidenced by the lower CD in Table 3 and the finer details in Fig. 11, our method clearly outperforms this baseline in both efficiency and mesh quality.

## 5. Conclusions

In this paper, we propose SNSR, a novel multi-scale representation to address the multi-view normal inconsistency that arises from varying scales when normal maps are observed under different camera-to-object distances. Furthermore, we introduce SMEM, which adaptively generates a scale-dependent surface based on the observation. Experiments demonstrate that our method achieves high-fidelity surface reconstruction from normals under both regular and close-up settings.

### 5.1. Limitation

Discontinuities appear on surfaces, such as the wings and face of *Angel* in Fig. 8. This issue may arise because our method relies on multi-resolution hash grids and analytical gradients. As a result, optimization updates propagate only within local hash grids, leading to a lack of non-local smoothness [LME\*23]. This problem could potentially be mitigated using the curvature loss proposed in [LME\*23], but as it involves second-order derivatives, the computational cost increases significantly. We leave the exploration of this direction to future work.

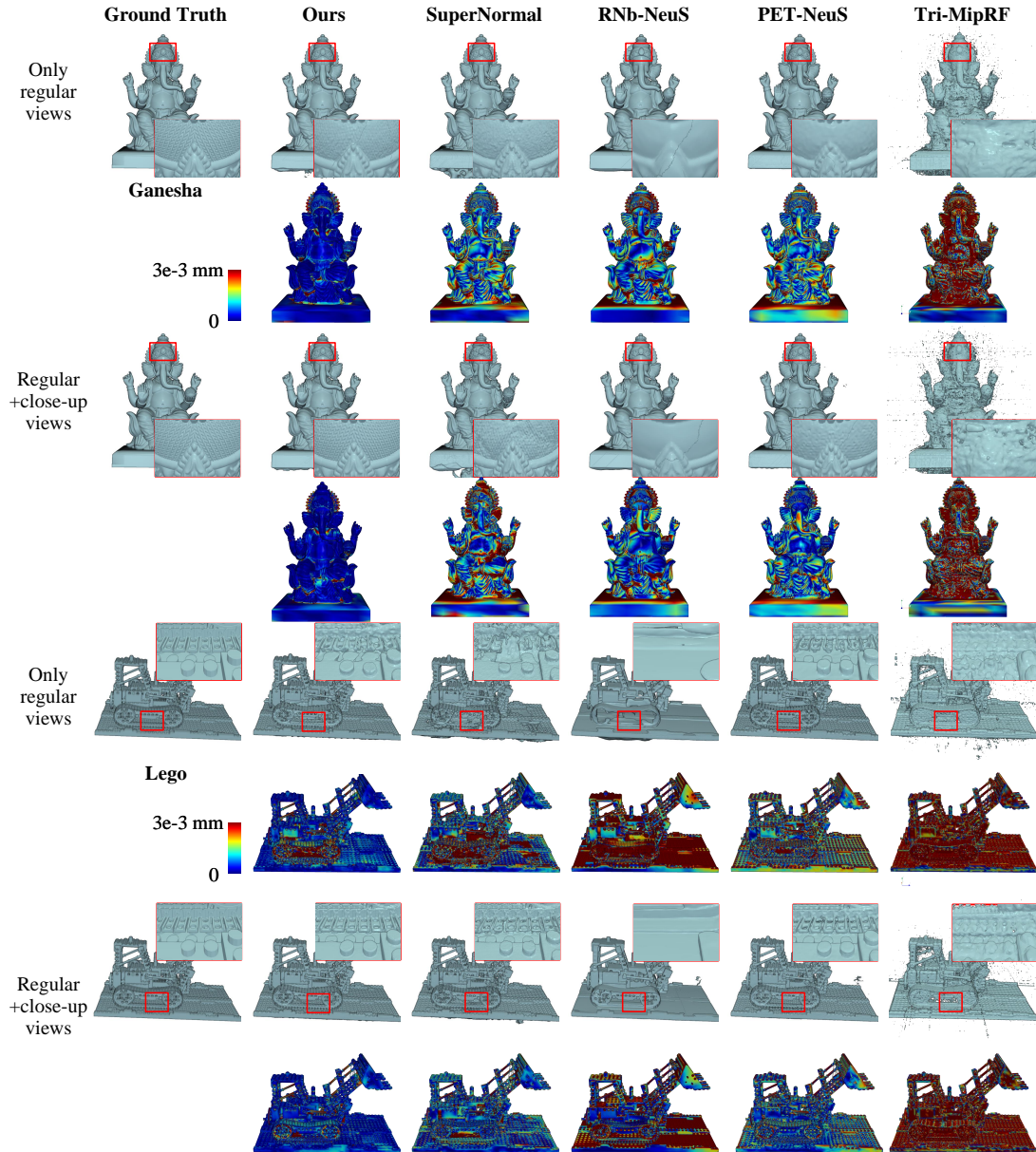
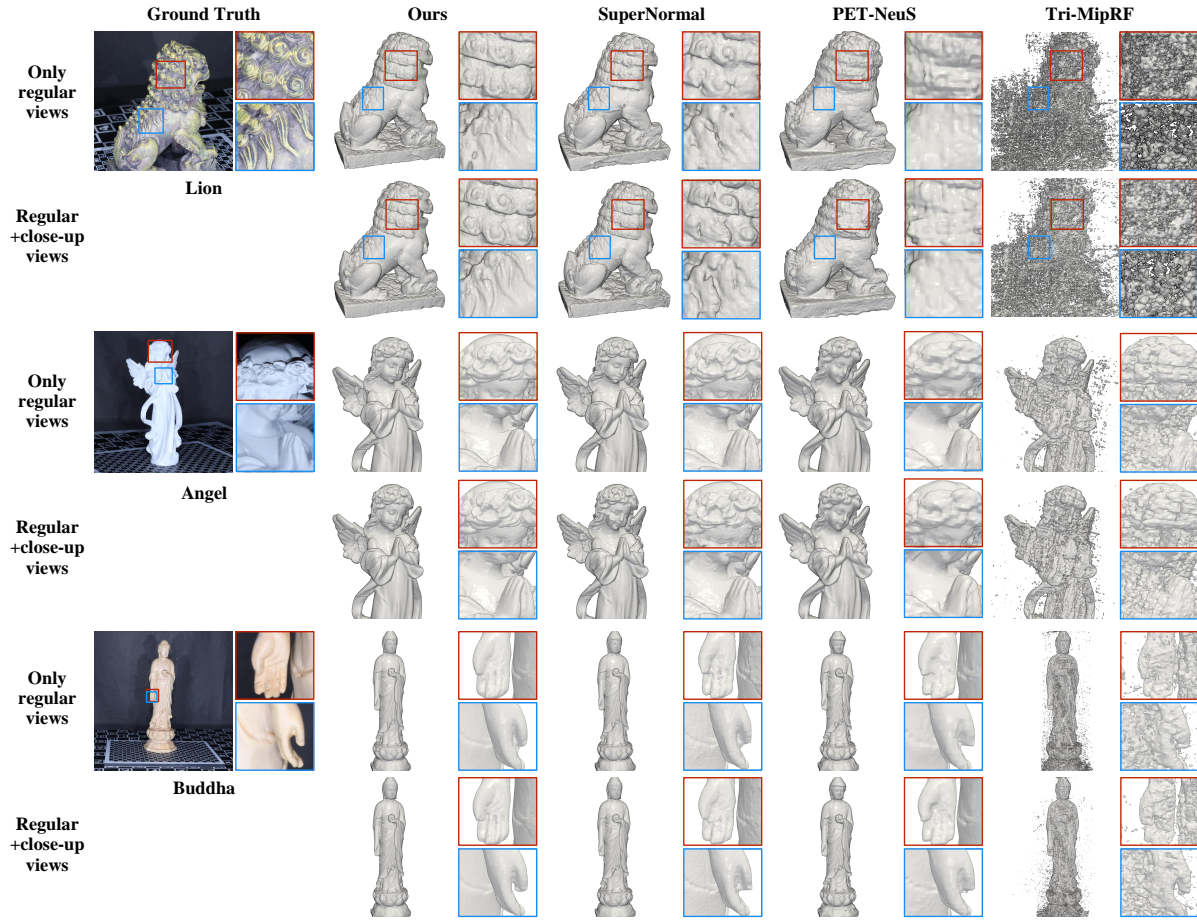


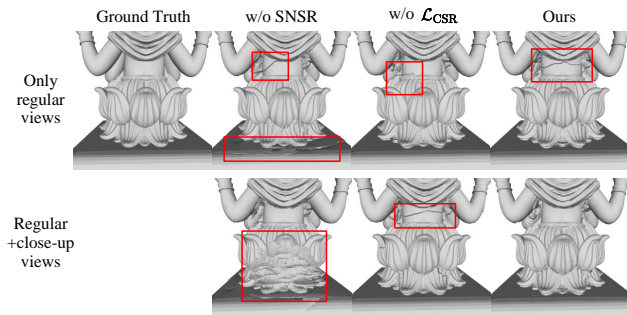
Figure 7: Comparison between our method and baselines on synthetic data.

Table 3: Quantitative comparison between using a globally consistent scale and the proposed SMEM. Values report the CD, with bold indicating the best results.

	Setting I, only regular views				Setting II, regular + close-up views			
	Ganesha	Lego	Mic	Ship	Ganesha	Lego	Mic	Ship
Consistent scale	0.0653	0.1488	0.0845	<b>0.0687</b>	0.0541	0.1324	0.0909	0.0719
SMEM	<b>0.0617</b>	<b>0.1474</b>	<b>0.0812</b>	0.0704	<b>0.0483</b>	<b>0.1131</b>	<b>0.0809</b>	<b>0.0684</b>



**Figure 8:** Comparison between our method and baselines on real-world data. (I) corresponds to Setting I, and (II) corresponds to Setting II. We zoom in on regions covered by close-up views and highly recommend that readers enlarge the figure to observe the differences clearly.



**Figure 9:** Qualitative comparisons on Ganesha between our method and those without the proposed SNSR or  $\mathcal{L}_{CSR}$ .

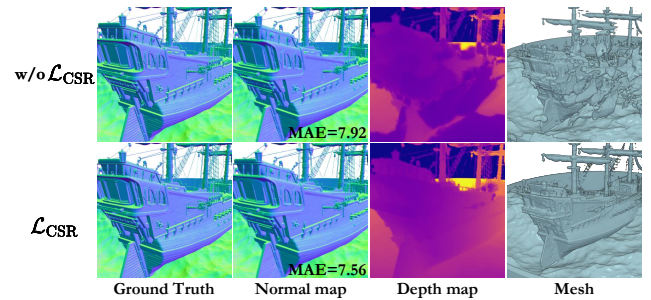


**Figure 10:** Qualitative comparison of the Ship results with and without  $\mathcal{L}_{CSR}$ .

### Acknowledgments

This work was supported the Beijing Key Laboratory of Multimodal Data Intelligent Perception and Governance, the Major Program of the National Natural Science Foundation of China

(No. 62495085), the National Natural Science Foundation of China (No. 62442603, 62472044, U24B20155), the Key Research and Development Program of Liaoning Province (No. 2023JH26/10200014), the Beijing Major Science and Technology Project (No. Z251100007125021), the Hebei Natural Science

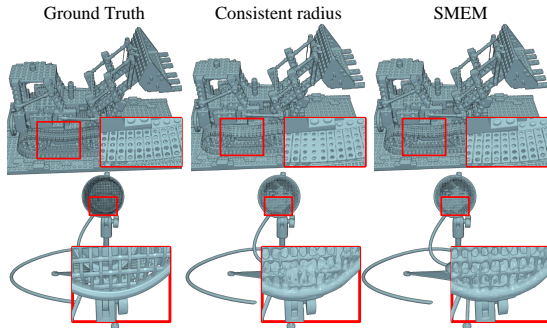


**Figure 11:** Qualitative comparisons of mesh extraction with and without SMEM in Setting II (regular + close-up views).

Foundation Project (No. 242Q0101Z), the Beijing-Tianjin-Hebei Basic Research Funding Program (No. F2024502017), and the Program of China Scholarship Council (No. 202306060184).

### Ethics Statement

We did not conduct any experimental work with human participants or animals that would require an ethics approval or participant/patient consent.

### References

- [Agi24] AGISOFT LLC: Agisoft metashape. <https://www.agisoft.com>, 2024. Accessed: 2025-09-13. 7
- [BBQ\*24] BRUMENT B., BRUNEAU R., QUÉAU Y., MÉLOU J., LAUZE F., DUROU J.-D., CALVET L.: Rnb-neus: Reflectance and normal-based multi-view 3d reconstruction. In *Proc. of IEEE Conference on Computer Vision and Pattern Recognition (CVPR)* (2024). 1, 3, 7, 8
- [BMT\*21] BARRON J. T., MILDENHALL B., TANCIK M., HEDMAN P., MARTIN-BRUALLA R., SRINIVASAN P. P.: Mip-nerf: A multiscale representation for anti-aliasing neural radiance fields. In *Proc. of International Conference on Computer Vision (ICCV)* (2021). 1, 3
- [BMV\*23] BARRON J. T., MILDENHALL B., VERBIN D., SRINIVASAN P. P., HEDMAN P.: Zip-nerf: Anti-aliased grid-based neural radiance fields. In *Proc. of International Conference on Computer Vision (ICCV)* (2023). 1, 3
- [CSS\*22] CAO X., SANTO H., SHI B., OKURA F., MATSUSHITA Y.: Bilateral normal integration. In *Proc. of European Conference on Computer Vision (ECCV)* (2022), Springer, pp. 552–567. 2
- [D.] D. L.: Sketchfab. <https://sketchfab.com/3d-models/lord-ganesh-1399da994ce54420878133a81f2f8f1e>. 6
- [DC07] DUROU J.-D., COURTEILLE F.: Integration of a normal field without boundary condition. In *Proc. of International Workshop on Photometric Analysis for Computer Vision* (2007), pp. 1–8. 2
- [FKMW\*23] FRIDOVICH-KEIL S., MEANTI G., WARBURG F. R., RECHT B., KANAZAWA A.: K-planes: Explicit radiance fields in space, time, and appearance. In *Proc. of IEEE Conference on Computer Vision and Pattern Recognition (CVPR)* (2023). 4
- [HB86] HORN B. K., BROOKS M. J.: The variational approach to shape from shading. *Computer Vision, Graphics, and Image Processing* 33, 2 (1986), 174–208. 2
- [HBZ25] HEEP M., BEHNKE S., ZELL E.: Feature-preserving mesh decimation for normal integration. In *Proc. of IEEE Conference on Computer Vision and Pattern Recognition (CVPR)* (2025), pp. 5783–5792. 3
- [HWM\*23] HU W., WANG Y., MA L., YANG B., GAO L., LIU X., MA Y.: Tri-miprf: Tri-mip representation for efficient anti-aliasing neural radiance fields. In *Proc. of International Conference on Computer Vision (ICCV)* (2023). 1, 3, 4, 7, 8
- [HYC\*24] HUANG B., YU Z., CHEN A., GEIGER A., GAO S.: 2d gaussian splatting for geometrically accurate radiance fields. In *Proc. of SIGGRAPH* (2024), pp. 1–11. 3
- [HZ24] HEEP M., ZELL E.: An adaptive screen-space meshing approach for normal integration. In *Proc. of European Conference on Computer Vision (ECCV)* (2024). 2, 3
- [Ike23] IKEHATA S.: Scalable, detailed and mask-free universal photometric stereo. In *Proc. of IEEE Conference on Computer Vision and Pattern Recognition (CVPR)* (2023), pp. 13198–13207. 6, 7
- [KKLD23] KERBL B., KOPANAS G., LEIMKÜHLER T., DRETTAKIS G.: 3d gaussian splatting for real-time radiance field rendering. *ACM Transactions on Graphics* 42, 4 (2023). 3
- [KKO\*22] KAYA B., KUMAR S., OLIVEIRA C., FERRARI V., VAN GOOL L.: Uncertainty-aware deep multi-view photometric stereo. In *Proc. of IEEE Conference on Computer Vision and Pattern Recognition (CVPR)* (2022), pp. 12601–12611. 7
- [KMR\*23] KIRILLOV A., MINTUN E., RAVI N., MAO H., ROLLAND C., GUSTAFSON L., XIAO T., WHITEHEAD S., BERG A. C., LO W.-Y., ET AL.: Segment anything. In *Proc. of International Conference on Computer Vision (ICCV)* (2023), pp. 4015–4026. 7
- [KPL25] KIM J., PARK G., LEE S.: Multiview geometric regularization of gaussian splatting for accurate radiance fields. In *Computer Graphics Forum* (2025), Wiley Online Library, p. e70179. 1
- [KPZK17] KNAPITSCH A., PARK J., ZHOU Q.-Y., KOLTUN V.: Tanks and temples: Benchmarking large-scale scene reconstruction. *ACM Transactions on Graphics* 36, 4 (2017), 1–13. 7
- [LBTZ24] LV Z., BAO X., TANG Y., ZHAO J.: Tansr: Efficient 3d reconstruction with tetrahedral difference and feature aggregation. In *Computer Graphics Forum* (2024), vol. 43, Wiley Online Library, p. e15207. 1
- [LC98] LORENSEN W. E., CLINE H. E.: Marching cubes: A high resolution 3d surface construction algorithm. In *Seminal Graphics: Pioneering Efforts that Shaped the Field*. 1998, pp. 347–353. 5
- [LHY\*24] LIU J., HU W., YANG Z., CHEN J., WANG G., CHEN X., CAI Y., GAO H.-A., ZHAO H.: Rip-nerf: Anti-aliasing radiance fields with ripmap-encoded platonic solids. In *Proc. of SIGGRAPH* (2024). 1, 3
- [LME\*23] LI Z., MÜLLER T., EVANS A., TAYLOR R. H., UNBERATH M., LIU M.-Y., LIN C.-H.: Neuralangelo: High-fidelity neural surface reconstruction. In *IEEE Conference on Computer Vision and Pattern Recognition (CVPR)* (2023). 8
- [LWZ\*24] LI J., WEN Z., ZHANG L., HU J., HOU F., ZHANG Z., HE Y.: Gs-octree: Octree-based 3d gaussian splatting for robust object-level 3d reconstruction under strong lighting. In *Computer Graphics Forum* (2024), vol. 43, Wiley Online Library, p. e15206. 3
- [LZH\*24] LIANG Z., ZHANG Q., HU W., FENG Y., ZHU L., JIA K.: Analytic-splatting: Anti-aliased 3d gaussian splatting via analytic integration. In *Proc. of European Conference on Computer Vision (ECCV)* (2024). 3
- [LZW\*20] LI M., ZHOU Z., WU Z., SHI B., DIAO C., TAN P.: Multi-view photometric stereo: A robust solution and benchmark dataset for spatially varying isotropic materials. *IEEE Transactions on Image Processing* (2020), 4159–4173. 1
- [MESK22] MÜLLER T., EVANS A., SCHIED C., KELLER A.: Instant neural graphics primitives with a multiresolution hash encoding. *ACM Transactions on Graphics* 41, 4 (2022), 102:1–102:15. 1, 3, 6
- [MST\*20] MILDENHALL B., SRINIVASAN P. P., TANCIK M., BARRON J. T., RAMAMOORTHY R., NG R.: Nerf: Representing scenes as neural radiance fields for view synthesis. In *Proc. of European Conference on Computer Vision (ECCV)* (2020). 3, 6

- [OFP04] OSHER S., FEDKIW R., PIECHOR K.: Level set methods and dynamic implicit surfaces. *Applied Mathematical Sciences* 57, 3 (2004), B15–B15. [5](#)
- [PBP\*24] PETIT D., BOURGEOIS S., PAVEL D., GAY-BELLILE V., CHABOT F., BARTHE L.: Ring-nerf: Rethinking inductive biases for versatile and efficient neural fields. In *Proc. of European Conference on Computer Vision (ECCV)* (2024), Springer, pp. 148–164. [3](#), [7](#)
- [PCW\*25] PEI M., CAO X., WANG X., GUO H., MA Z.: Pmni: Pose-free multi-view normal integration for reflective and textureless surface reconstruction. In *Proc. of IEEE Conference on Computer Vision and Pattern Recognition (CVPR)* (2025), pp. 26834–26843. [3](#)
- [QDA18] QUÉAU Y., DUROU J.-D., AUJOL J.-F.: Normal integration: a survey. *Journal of Mathematical Imaging and Vision* 60 (2018), 576–593. [2](#)
- [WHH\*23] WANG Y., HAN Q., HABERMANN M., DANILIDIS K., THEOBALT C., LIU L.: Neus2: Fast learning of neural implicit surfaces for multi-view reconstruction. In *Proc. of International Conference on Computer Vision (ICCV)* (2023). [1](#)
- [WLL\*21] WANG P., LIU L., LIU Y., THEOBALT C., KOMURA T., WANG W.: Neus: Learning neural implicit surfaces by volume rendering for multi-view reconstruction. In *Proc. of Annual Conference on Neural Information Processing Systems (NeurIPS)* (2021). [3](#), [5](#)
- [WRG\*23] WANG F., REN J., GUO H., REN M., SHI B.: Diligent-pi: A photometric stereo benchmark dataset with controlled shape and material variation. In *Proc. of International Conference on Computer Vision (ICCV)* (2023), pp. 9477–9487. [1](#)
- [WSW22] WANG Y., SKOROKHOV I., WONKA P.: Hf-neus: Improved surface reconstruction using high-frequency details. In *Proc. of Annual Conference on Neural Information Processing Systems (NeurIPS)* (2022), vol. 35, pp. 1966–1978. [3](#)
- [WSW23] WANG Y., SKOROKHOV I., WONKA P.: Pet-neus: Positional encoding triplanes for neural surfaces. In *Proc. of IEEE Conference on Computer Vision and Pattern Recognition (CVPR)* (2023). [3](#), [7](#), [8](#)
- [XT24] XU C., TAKAFUMI T.: Supernormal: Neural surface reconstruction via multi-view normal integration. In *Proc. of IEEE Conference on Computer Vision and Pattern Recognition (CVPR)* (2024). [1](#), [2](#), [3](#), [6](#), [7](#), [8](#)
- [YCH\*24] YU Z., CHEN A., HUANG B., SATTTLER T., GEIGER A.: Mip-splatting: Alias-free 3d gaussian splatting. In *Proc. of IEEE Conference on Computer Vision and Pattern Recognition (CVPR)* (2024), pp. 19447–19456. [3](#)
- [ZYW25] ZHU Z.-L., YANG J., WANG B.: Gaussian splatting with discretized sdf for relightable assets. [3](#)
- [ZZF\*23] ZHUANG Y., ZHANG Q., FENG Y., ZHU H., YAO Y., LI X., CAO Y.-P., SHAN Y., CAO X.: Anti-aliased neural implicit surfaces with encoding level of detail. In *Proc. of SIGGRAPH Asia* (2023). [3](#), [7](#)